3D modelling of misfit networks in the interface region of heterostructures

2007 J. Phys. D: Appl. Phys. 40 4084

(http://iopscience.iop.org/0022-3727/40/13/027)

IOP Publishing Journal of Physics D: Applied Physics
J. Phys. D: Appl. Phys. **40** (2007) 4084–4091 doi:10.1088/0022-3727/40/13/027

3D modelling of misfit networks in the interface region of heterostructures

Toby D Young[1], Joseph Kioseoglou[2], George P Dimitrakopulos[2], Paweł Dłużewski[1] and Philomela Komninou[2]

[1] Institute of Fundamental Technological Research, Polish Academy of Science, ul. Swiętokryska 21, 00-049 Warsaw, Poland
[2] Department of Physics, Aristotle University of Thessaloniki, GR-54124 Thessaloniki, Greece

E-mail: tyoung@ippt.gov.pl

Received 5 January 2007, in final form 27 April 2007
Published 15 June 2007
Online at stacks.iop.org/JPhysD/40/4084

Abstract
We present a methodology for the stress–strain analysis of a film/substrate interface by combining crystallographic and continuum modelling. Starting from measurements of lattice parameters available from experimental observations, the heterostructure is recast initially in the form of a crystallographic model and finally as a continuum elastic model. The derived method is capable of handling dense arrays of misfit dislocations as well as large areas of the interface between two crystal structures. As an application we consider the misfit dislocation network in the GaN/Al_2O_3 interface region through determination of strain relaxation and associated residual stresses. Our calculated results are referred back to and found to be in good agreement with the experimental observations of misfit dislocation arrays obtained from high resolution transmission electron microscopy.

(Some figures in this article are in colour only in the electronic version)

1. Introduction

In epitaxial material systems, such as III–V semiconductors, structural defects and the associated residual strain are in part instrumental for the manipulation of their physical responsive properties and ultimately the efficiency of technological devices. Defects usually degrade device performance (e.g. [1, 2]), and innovative techniques are constantly developed in order to understand, manipulate, and reduce defect content (e.g. [2–5]).

A very potent origin of defects is the 'mismatch' between a deposited layer and its substrate that arises due to differences of symmetry and structure. The most common type of mismatch is lattice mismatch (i.e. the mismatch between the translation symmetry), which is accommodated for epitaxial films with thickness greater than critical by misfit dislocations (e.g. [3, 6]). Other differences between the structures of adjacent crystals may also lead to defect introduction [7, 8]. Using topological arguments an expression that characterizes all of the potential defects, which can arise in this manner, has been obtained [7, 8]. For this purpose the Volterra description for the characterization of line defects in elastic continua has been extended to interfacial defects in bicrystals. In this respect the employed operations in the Volterra approach are defined by the symmetry and structure of the participating crystals.

Despite its usefulness for the *a priori* determination of admissible interfacial defects and for the description of topological parameters such as the Burgers vectors, topological analysis of interfaces does not yield information on energetically preferable configurations. For such purposes it is required to employ an energetic calculation method for which the topological model is the starting configuration. However, in the case of methods involving interatomic interactions (e.g. molecular dynamics with empirical potentials or *ab initio* methods) there are serious problems when distinct crystals are involved (i.e. heterophase epitaxy) or compound crystals requiring complicated interatomic interactions. In addition, it is always a problem to study large areas of interface, involving several hundred thousand or even millions of atoms, and complex defect interactions, due to the significant demand on computational power. So, to our knowledge, it is currently not possible to study the distribution of strains and stresses in a bicrystal for a large and dense network of misfit dislocations.

In the present work we propose a novel methodology for the study of the stress and strain fields generated by a network of dense misfit dislocations, using continuum modelling by nonlinear elasticity and the finite elements (FE) method. We show how it is possible to employ the topological model of a bicrystal as input for such analysis by continuum mechanics. Using a case study we also demonstrate satisfactory agreement of the obtained results with the experimental observations. Since the actual atomic positions are not relevant for such modelling, we avoid the need to define the interatomic interactions and we are also capable of treating large 3D volumes of material in order to obtain stress and strain fields in epitaxial systems. The obtained information should be invaluable in assessing the impact of stress–strain distribution on various material properties such as for example the optoelectronic properties of compound epitaxial semiconductors.

The aim of this work is to achieve a reciprocal relation between continuum modelling and the atomistic scale by illustrating the generation of the 3D strain and stress fields associated with a dense network of misfit dislocations and confirming this result by experimental observations. Starting from the topological bicrystal we aim to build a 3D model of the strain and related residual stress response in the interface region between film and substrate. It may then be possible to investigate such a system in terms of its effectiveness in technological applications and devices.

As a case study we employ that of (0 0 0 1) GaN on sapphire (Al_2O_3). This system has a relatively high misfit dislocation density and is also very important technologically. Sapphire and silicon carbide are up-to-now two preferred substrates for the growth of III-N compound semiconductor layers primarily because of the hexagonal symmetry they provide and as well as their relatively good lattice and thermal mismatch with the epilayer. Epitaxial growth of III-N/Al_2O_3 film/substrate heterostructures has received significant attention in recent years (e.g. [1, 2]). Misfit dislocations in the (0 0 0 1) GaN/Al_2O_3 system find their origin in the large lattice mismatch. It is therefore of interest to understand the strain relaxation in the III-N film and in particular with respect to a high density of misfit dislocations. Furthermore, threading dislocations are associated to the misfit dislocations and thus an understanding of the arrangements of misfit dislocation networks is of interest [9].

This paper is organized as follows: in section 2 the methodology followed is outlined, and in section 3 the important tool of geometrical phase analysis (GPA) [10] is briefly reviewed. In section 4, the experimental observations by high resolution transmission electron microscopy (HRTEM) and the crystallographic modelling are described. In section 5, we describe our method of relaxation process of the strain energy by descritizing space with the FE method. We turn to a verification of our method in section 6 by comparing the theoretical relaxed strain distribution with that derived from the experimental observations. The conclusions are discussed in section 7.

2. Methodology

The case of the relaxation of strain energy in the GaN/Al_2O_3 interfacial region studied here is by the formation of a network

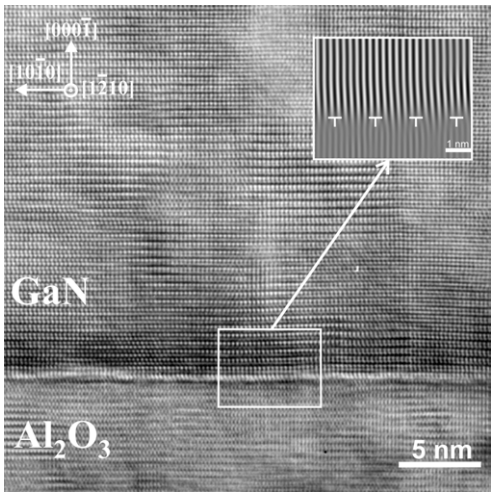

Figure 1. HRTEM image along the $[1\,\bar{2}\,1\,0]_{GaN}$ of the GaN/Al_2O_3 epitaxial interface (thickness 2.2 nm, defocus −0.59 nm, white spots represent atomic columns). The inset gives the Bragg image of $(1\,0\,\bar{1}\,0)_{GaN}/(1\,\bar{1}\,\bar{1}\,0)_{Al_2O_3}$ lattice plane periodicities obtained after FFT filtering of the corresponding spatial frequencies.

of three arrays of 60° mixed-type misfit dislocations crossing at $2\pi/3$ rad [9]. We analyse this case in three conjoined steps of modelling. In the first step the dichromatic complex and the 3D unrelaxed bicrystal, containing a few misfit dislocations, are obtained using lattice constants obtained from experimental observations by HRTEM. The 3D FE mesh is then constructed in agreement with the bicrystal symmetry in such a way as to obtain a sample of reasonable size with a number of dislocation nodes trapped inside thus forming a complex network of misfit dislocations. For facilitating the transition from the atomistic scale to continuum modelling by FE analysis, a map of the reduced relative displacement of GaN with respect to Al_2O_3 is generated from the unrelaxed bicrystal using GPA. Since displacement fields obtained by GPA are 2D, a procedure for extending them to 3D is established. This initial field is then applied to the FE mesh. The FE algorithm is applied on the basis of nonlinear elasticity. The obtained results are finally compared, through GPA, to HRTEM experimental observations of the (0 0 0 1) GaN/Al_2O_3 interface.

3. Brief review of GPA

The experimental conditions of the micrograph in figure 1 were determined by comparison with a calculated 'through-focus-thickness' map using electron microscopy simulation (EMS) [11] resulting in simulated images with a resolution of 4096 × 4096 pixels. GPA was then employed to obtain Bragg images and distortion fields from the simulated micrographs.

In electron diffraction, diffracted beams have an associated phase and amplitude. By performing a Fourier transform on a HRTEM image it is possible to obtain the phase component of areas of interest. For this purpose a mask (e.g. Gaussian, Lorentzian) is applied to the periodicity of interest in order to isolate the respective phase component. The phase P_g is related to the displacement field by the expression [10]

$$P_g(\boldsymbol{r}) = -2\boldsymbol{g}\cdot\boldsymbol{u}(\boldsymbol{r}), \tag{1}$$

Table 1. Crystallographic and structural data for trigonal-hexagonal Al_2O_3 and wurtzite GaN. Lengths a, c are given in Å and the elastic constants C_{ij} in GPa. The parameters for GaN are taken from [14] and for Al_2O_3 from [15].

	a	c	C_{11}	C_{12}	C_{13}	C_{33}	C_{44}
GaN	3.1466	5.19	396	137	108	373	116
Al_2O_3	4.76	12.99	497.0	162.2	114.9	502.3	147.4

and the local distortions of the lattice are measured from the deformation field $\boldsymbol{e}$ which is related to the displacement field $\boldsymbol{u}(\boldsymbol{r})$ according to

$$\boldsymbol{e} = \begin{pmatrix} \boldsymbol{e}_{xx} & \boldsymbol{e}_{xy} \\ \boldsymbol{e}_{yx} & \boldsymbol{e}_{yy} \end{pmatrix} = \begin{pmatrix} \partial \boldsymbol{u}_x/\partial \boldsymbol{x} & \partial \boldsymbol{u}_x/\partial \boldsymbol{y} \\ \partial \boldsymbol{u}_y/\partial \boldsymbol{x} & \partial \boldsymbol{u}_y/\partial \boldsymbol{y} \end{pmatrix}, \tag{2}$$

and rotation

$$\boldsymbol{r}_{xy} = \tfrac{1}{2}(\boldsymbol{e}_{xy} - \boldsymbol{e}_{yx}), \tag{3}$$

to obtain 2D lattice strain and rotation maps corresponding to the given HRTEM image.

In figures 8(*a*) and (*b*) the $\boldsymbol{e}_{xx}$, $\boldsymbol{e}_{xy}$ and $\boldsymbol{r}_{xy}$ distortion components obtained from the experimental image by GPA are given, respectively. The GPA strain and rotation components are presented here for a $\boldsymbol{g}/4$ Gaussian mask. Similar information was obtained from the crystallographic model as described in section 4.2.

4. Experimental observations and crystallography

4.1. HRTEM observations

HRTEM provides a suitable method with which to quantitatively probe the details of lattice displacements up to sub-angstrom accuracy [12]. In this work experimental observations were performed using a JEOL 2011 electron microscope (point resolution 0.19 nm, Cs = 0.5 nm). Observations were performed in cross-section along $\langle 1\,\bar{2}\,1\,0\rangle$ in GaN epitaxial layers grown on (0 0 0 1) sapphire by rf plasma-assisted molecular beam epitaxy (rf-MBE) [13]. HRTEM image simulations were performed using the multislice algorithm of the EMS software [11]. The experimental conditions of thickness and defocus were identified by comparison with simulated through-focus-thickness images of perfect GaN.

In the HRTEM micrograph of figure 1 the (0 0 0 1) GaN/Al_2O_3 interface is depicted viewed along the $[1\,\bar{2}\,1\,0]$ zone axis of GaN. The relative orientation relationship of the two crystals is $(0\,0\,0\,1)_{GaN}/(0\,0\,0\,1)_{Al_2O_3}$, $[1\,\bar{2}\,1\,0]_{GaN}/[1\,\bar{1}\,0\,0]_{Al_2O_3}$. The $[1\,0\,\bar{1}\,0]$ d-spacing of GaN is determined experimentally from figure 1 to be $d = 0.2725$ nm, taking as reference the well-defined lattice constant of Al_2O_3. This yields a GaN lattice parameter of $a = 0.314\,66$ nm. The lattice mismatch between crystal layers is defined by the simple relation $f = (a_{epi} - a_{ref})/a_{ref}$ where a_{epi} and a_{ref} denote the epitaxial and reference lattice constants, respectively. Taking Al_2O_3 as reference the lattice mismatch for parallel-oriented crystals is $f = 0.3388$. The relative rotation of $\pi/3$ rad significantly reduces the lattice mismatch to $f = 0.1452$. Since it is of interest to understand the effects of relatively optimal, though high, dislocation density and with a view toward technologically practicable devices, the latter configuration is investigated in this work.

The c lattice parameter of GaN is influenced by the biaxial strain in agreement with the well-known equation $\varepsilon_3 = -2(C_{13}/C_{33})$, where $\varepsilon_1 = (a_{exp}/a_{GaN}) - 1$ and $\varepsilon_3 = (c_{cal}/c_{GaN}) - 1$. In the above equations, c_{GaN} and a_{GaN} are the lattice constants of relaxed GaN ($a_{GaN} = 0.3189$ nm $c_{GaN} = 0.5185$ nm), $a_{exp} = 0.314\,66$ nm is the in-plane lattice constant measured on the HRTEM micrograph, and C_{13}, C_{33} are elastic constants (see table 1). By assuming pure biaxial strain, the c lattice parameter is calculated to be $c_{cal} = 0.520\,25$ nm. Experimentally the same parameter was determined to be $c_{exp} = 0.519$ nm. The small difference between c_{cal} and c_{exp} could be due, apart from possible experimental error, to a small additional hydrostatic or uniaxial strain component. Such a component will be ignored in the following without significant influence on the outcome of the calculation.

Using filtering in Fourier space it is possible to isolate the $[1\,0\,\bar{1}\,0]_{GaN}$ and $[\bar{1}\,\bar{1}\,2\,0]_{Al_2O_3}$ spatial frequencies in order to visualize the edge component of misfit dislocations in the form of terminating fringes of substrate lattice planes (figure 1). In this manner only one array of misfit dislocations is visualized. For complete misfit relaxation, three arrays of 60° mixed-type misfit dislocations, crossing at 2 /3 rad, are required due to the common symmetry of the two crystals as shown experimentally elsewhere [16]. The misfit dislocations have Burgers vectors $\boldsymbol{b} = 1/\langle 2\,\bar{1}\,\bar{1}\,0\rangle$ with respect to GaN and comprise an edge component $\boldsymbol{b}_e = 1/2\langle 1\,0\,\bar{1}\,0\rangle$ and a screw component $\boldsymbol{b}_s = 1/6\langle 1\,\bar{2}\,1\,0\rangle$.

4.2. Topological bicrystal

The topological methodology developed by Pond and co-workers [7, 8, 16] is employed here in order to construct the GaN/Al_2O_3 bicrystal. The GaN lattice parameters determined by HRTEM (taking the Al_2O_3 lattice parameters to be known) are used for this purpose. These values are listed in table 1.

For the topological analysis of a bicrystal, the dichromatic pattern, i.e. the 3D composite of interpenetrating lattices, is first constructed and its symmetry determined [9]. In the second step we consider the actual crystal structures to interpenetrate thus yielding the dichromatic complex [16]. Finally, the unrelaxed bicrystal is obtained by defining the interfacial orientation and discarding one crystal on either side of the interface. A well-defined disymmetrization procedure is followed in these three steps yielding finally the bicrystal layer symmetry.

For our case the GaN and Al_2O_3 space groups are $P6_3mc$ and $R\bar{3}c$, respectively. The symmetry exhibited by the dichromatic pattern is $P3m$. This composite is illustrated schematically in figure 2(*a*). The coincident lattice translations in the basal plane correspond to $7/3\langle 2\,\bar{1}\,\bar{1}\,0\rangle_{GaN}$. Going

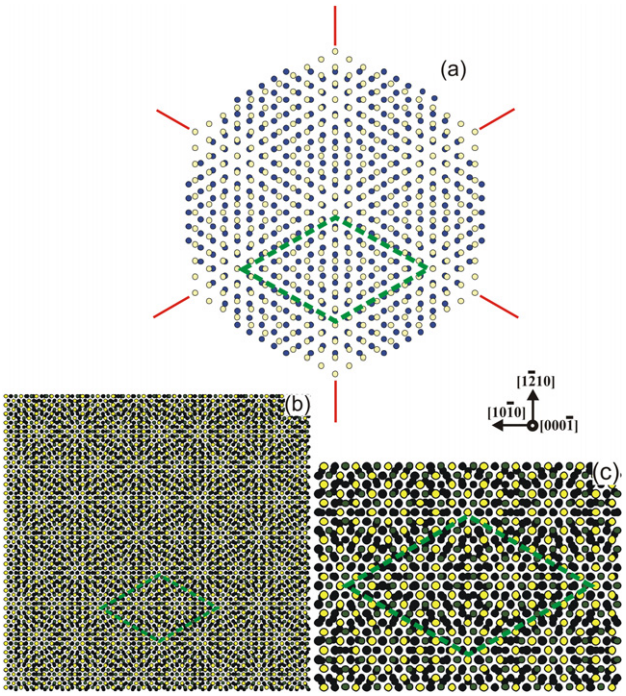

Figure 2. (*a*) Schematic illustration along [0 0 0 1] of the dichromatic pattern obtained from two hexagonal lattices that have been relatively rotated by $\pi/3$ about [0 0 0 1]. The primitive unit-cell and the directions of the misfit dislocations are indicated. (*b*) Schematic illustration along [0 0 0 1] of the corresponding dichromatic complex obtained from wurtzite GaN and Al_2O_3. The primitive unit-cell is again indicated. (*c*) Enlarged view of the primitive unit-cell. Large and small circles denote distinct atomic species; shading of atoms denotes various levels along the projection direction.

now to the dichromatic complex (figure 2(*b*)), the coincident symmetry is reduced to $P3$ and the 2D bicrystal symmetry that is finally obtained for the (0 0 0 1) interface is $p3$. By admitting one misfit dislocation in each primary unit-cell the layer symmetry is further reduced to $p1$. There are three variants given by the coset analysis $p3 = \{\mathrm{I}, 3^+, 3^-\} \cup p1$ (where I is the identity operation, and $3^{\pm}$ denote the $\pm 2\pi/3$ rotations about [0 0 0 1]), corresponding to the three arrays of misfit dislocations. Figure 3 illustrates schematically the primary unit-cell given in figure 2. Rotation around the 3-fold axis (black closed triangles in figure 3(*a*) gives rise to misfit dislocation variants. The unit-cell is sequentially translated by the coincident periodicity to obtain a honeycomb network of misfit dislocations depicted in figure 3(*b*). The full structure is then employed for construction of a FE mesh in the manner described in section 5.

Figure 4(*a*) illustrates the unrelaxed bicrystal viewed along $[1\,\bar{2}\,1\,0]_{\mathrm{GaN}}$, i.e. the same projection direction as that of the experimental image of figure 1. In figure 4(*b*) the simulated HRTEM image obtained from figure 4(*a*) is given. For the simulation, the experimental conditions of the micrograph in figure 1 was employed in EMS. Simulations were obtained at a resolution of 4096 × 4096 pixels. GPA was employed on the HRTEM image simulation of figure 4(*b*) to obtain distortion fields from the crystallographic model aiming to be used as input for the FE method. In figures 4(*c*) and (*d*) the Bragg images from Fourier filtering along [0 0 0 2] and [1 0 $\bar{1}$ 0] are given, respectively. In figures 4(*e*)–(*g*) the $\boldsymbol{e}_{xx}$, $\boldsymbol{e}_{xy}$ and $\boldsymbol{r}_{xy}$ distortion components obtained from GPA are given, respectively. The GPA strain and rotation components are presented here for a $g/4$ Gaussian mask.

It should be noted that, although the topological bicrystal is unrelaxed, a one-to-one correspondence between substrate and epilayer lattice planes can be defined leading to the emergence of extra half-planes in agreement with the misfit dislocation periodicity. Then the reduced relative displacements between corresponding lattice planes constitute the displacement field obtained by GPA. This initial displacement field is a satisfactory starting point for the further application of FE analysis by nonisotropic elasticity. Note that extra half-planes in the crystallographic model give rise to dislocation-like contrast in the GPA maps. However, the distribution of the strain around such points should be corrected through the FE algorithm.

The GPA strain contrast in figures 4(*e*)–(*g*) is mainly localized at the dislocation positions. Of course a longer range displacement field also appears denoted mainly by the change of colour between substrate and epilayer in the $\boldsymbol{e}_{xx}$ map. This contrast is due to the difference in the lattice parameters of the two materials and the use of one of the two as reference space. So it should not be confused with the actual existence of any long-range elastic deformation. On the contrary, for the construction of the crystallographic model it has been assumed that the structure is fully relaxed, i.e. the elastic strain is fully absorbed by the misfit dislocations. Any residual elastic strain would be expected to be manifest by a modification of the spacing of the misfit dislocations in the experimental image, which is not the case.

5. Finite element modelling of misfit dislocations

5.1. Relaxation of the strain energy

The lattice distortion maps of figures 8(*a*) and (*b*) derived from the micrograph of figure 1, show nonlinear elastic behaviour manifest as an asymmetry between regions of compression and extension formed around the dislocation core. For this reason the traditional approach based on linear elasticity is replaced here by a *nonlinear* elastic theory, reviewed in detail elsewhere [17–19], developed so as to describe the nonlinear behaviour of materials on the nanoscale; see also e.g. [20]. In this way we aim to better take into account the observed nonlinearity in the vicinity of dislocations.

The micrographs of figures 1 and 4 provide the lattice reference configuration of the heterostructure. We distinguish between three principal components that together contribute to the total deformation of the elastic crystal. First, the source deformation field assumed to determine the lattice distortion field for the entire heterostructure; secondly, a chemical deformation gradient describing the transition between perfect lattices of Al_2O_3 and GaN; and thirdly, the lattice deformation gradient determined by GPA in relation to some region of Al_2O_3 chosen to be the reference region to measure the deformation map for the whole structure visible on the HRTEM image.

The total deformation gradient $\boldsymbol{F}$ is decomposed therefore into three components:

$$\boldsymbol{F} = \boldsymbol{F}_{\mathrm{e}}\boldsymbol{F}_{\mathrm{ch}}\boldsymbol{F}_{\circ}, \tag{4}$$

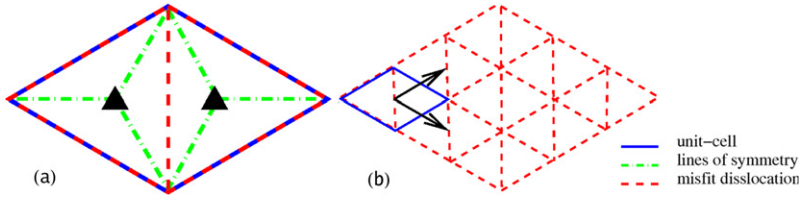

Figure 3. (*a*) Schematic representation of coset decomposition of the primitive unit-cell employed here, cf figures 2(*c*). (*b*) Construction of the resultant initial honeycomb misfit dislocation pattern through translation of the primitive unit-cell by the coincidence periodicity. Solid lines give the boundary of a unit-cell and dashed lines denote misfit dislocations. Dash-dot lines in (*a*) mark out boundaries of the sub-cells with point rotational symmetry.

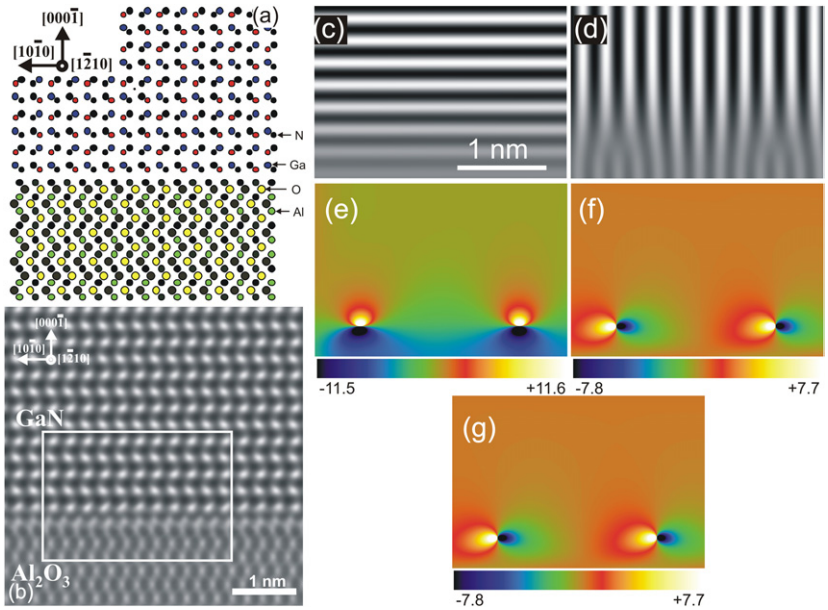

Figure 4. In the left panel: (*a*) schematic illustration along $[1\,\bar{2}\,1\,0]_{GaN}$ of the unrelaxed bicrystal between GaN and Al_2O_3. (*b*) Corresponding HRTEM image simulation under the same thickness and defocus conditions as in figure 1. In the right panel, measurements taken from the white bounding box in (*b*). In particular, (*c*) and (*d*) are the Bragg images from Fourier filtering with [0 0 0 2] and $[1\,0\,\bar{1}\,0]_{GaN}/[\bar{1}\,\bar{1}\,2\,0]_{Al_2O_3}$ frequencies. Distortion components (*e*) $\boldsymbol{e}_{xx}$, (*f*) $\boldsymbol{e}_{xy}$ and (*g*) $\boldsymbol{r}_{xy}$.

where $\boldsymbol{F}_e$, $\boldsymbol{F}_{ch}$ and $\boldsymbol{F}_\circ$ are the elastic, chemical and initial lattice deformation tensors, respectively. The chemical deformation tensor in Al_2O_3 is taken to be the unit tensor. The source and total deformation tensors are related to the distortion field $\boldsymbol{e}(\boldsymbol{r})$ and displacement vector field $\boldsymbol{u}(\boldsymbol{r})$ derived from GPA by the following relations:

$$\boldsymbol{F}_0^{-1} = \boldsymbol{I} - \boldsymbol{e}, \tag{5}$$

$$\boldsymbol{F}^{-1} = \boldsymbol{I} - \nabla\boldsymbol{u}, \tag{6}$$

where $\boldsymbol{I}$ is the unit matrix. The continuum model used here is based on the integration of the equilibrium condition on the Cauchy stress tensor [21]

$$\nabla \cdot \boldsymbol{\sigma} = 0, \tag{7}$$

In terms finite strains, where the stress measure conjugate by work with the logarithmic strain is refers to the reference (undeformed) crystal lattice and satisfies the following linear constitutive equation

$$\hat{\boldsymbol{\sigma}} = \hat{\boldsymbol{c}} : \hat{\varepsilon}, \tag{8}$$

where a hat denotes the reference (undeformed) lattice configuration. Here $\hat{\varepsilon}$ is the Lagrangian logarithmic (i.e. nonlinear) strain tensor defined as $\hat{\varepsilon} = \ln(\boldsymbol{U})$, where $\boldsymbol{U}$ is the right stretch tensor of elastic deformation from the polar decomposition $\boldsymbol{F}_e = \boldsymbol{R}\boldsymbol{U}$ where $\boldsymbol{R}$ is the orthogonal rotation tensor. The fourth-order proper-symmetric tensor of elastic stiffness $\hat{\boldsymbol{c}}$ is assumed here to be a tensor of material constants; see table 1.

Due to nonlinear geometric changes between the reference and current lattice configurations, it can be shown that such constitutive equation leads to a nonlinear relation for the Cauchy stress

$$\boldsymbol{\sigma} = \boldsymbol{c} : \varepsilon, \tag{9}$$

where

$$\varepsilon = \mathcal{A}^{-\mathrm{T}} : \hat{\varepsilon}, \tag{10}$$

$$\boldsymbol{c} = \mathcal{A} : \hat{\boldsymbol{c}} : \mathcal{A}^{\mathrm{T}} \det(\boldsymbol{F}_e^{-1}), \tag{11}$$

$$\mathcal{A}^{ij}{}_{IJ} = R^i{}_K R^j{}_L \hat{\mathcal{A}}_{IJ}{}^{KL}, \tag{12}$$

the geometric transformation tensor $\hat{\mathcal{A}}$ is a function of elastic strain $\hat{\varepsilon}$, see [17], while the elastic strain depends on the total displacement field and source distortions. The result is that the Cauchy stress tensor $\boldsymbol{\sigma}$ is obtained as a nonlinear function of $\boldsymbol{u}$, $\nabla\boldsymbol{u}$ and $\boldsymbol{e}$.

Using the virtual work principle the following nonlinear matrix equation is found:

$$\boldsymbol{P}(\boldsymbol{a}) = \boldsymbol{f}, \tag{13}$$

where the vector $\boldsymbol{P}$ is a nonlinear function of nodal variables

$$\boldsymbol{P} = \begin{pmatrix} \int_v \nabla^{\mathrm{T}} \boldsymbol{W}\boldsymbol{\sigma}\,\mathrm{d}v \\ \boldsymbol{0} \end{pmatrix}, \tag{14}$$

$$\boldsymbol{a} = \begin{pmatrix} \boldsymbol{u} \\ \varepsilon \end{pmatrix}, \tag{15}$$

$$\boldsymbol{f} = \begin{pmatrix} \int_{\partial \boldsymbol{v}} \boldsymbol{W}\boldsymbol{\sigma}\,ds \\ \boldsymbol{0} \end{pmatrix}. \tag{16}$$

Here $\boldsymbol{W}$ denotes the weighting function determined in relation to the current (iterated) configuration. The nonsymmetric equation set (13) is solved for displacements on a finite element mesh using the Newton–Raphson method in which the tangent stiffness matrix takes the form $\boldsymbol{K} = \partial \boldsymbol{P}/\partial \boldsymbol{a}$ [21].

5.2. Reconstruction of 3D structure into FEA

A region of the GPA results (figures 4(*e*)–(*g*) corresponding to the misfit dislocation periodicity scaled to a resolution of 9×11 pixels is taken into theoretical analysis. The numerical value (of each pixel) of the distortion field are allowed to represent the initial strain value at each corner of a 27-node Lagrangian FE. The system is subsequently allowed to relax.

Scaling, which requires some form of interpolation, was achieved here using cubic maximal-order interpolation of minimal support (MOMS) [22]. This approach has one important advantage since the MOMS algorithm provides a scheme by which singularities arising in the dislocation core are effectively 'smoothed out' using a simple polynomial interpolation function. It is noted that this procedure introduces an uncertainty in the validity of the nonlinear elastic model in the immediate vicinity of the dislocation core related to the degree of smoothing used. This is of no great importance however since it is known that the theory of elasticity is unable to accurately take into account these regions without further information about atomic interactions.

For an extension from the 2D mapping of figure 4 to a 3D continuum model of the strain energy similar operations are applied on the distortion tensor $\boldsymbol{\epsilon}$ as were applied on the spatial coordinate system described in section 4.2; namely, rotations of $2\pi/3$ rad and translation by the coincidence periodicity. The distortion tensor (where $z \parallel c$) thus transforms as

$$\boldsymbol{e} \mapsto \tilde{\boldsymbol{e}} = \mathcal{R} \begin{pmatrix} \boldsymbol{e}_{xx} & 0 & \boldsymbol{e}_{xz} \\ \frac{\sqrt{2}}{2}\boldsymbol{e}_{xz} & 0 & \frac{\sqrt{2}}{2}\boldsymbol{e}_{zz} \\ \boldsymbol{e}_{zx} & 0 & \boldsymbol{e}_{zz} \end{pmatrix} \mathcal{R}^{\mathrm{T}} + \mathcal{T}, \tag{17}$$

where $\mathcal{R}$ and $\mathcal{T}$ are the well-known rotation and translation transformations for an $\mathbb{E}^3$ Cartesian coordinate system. The resultant FE mesh is given in figure 5, where the volume taken into account is $\sim 150\,\mathrm{nm}^3$ allows for the origin of nine misfit dislocations crossing at $2\pi/3$ rad.

6. Results

The GaN/Al_2O_3 system in the configuration of relaxed strain is given in figure 6. In the left panel the complete structure is given where the lines of the finite element mesh are displayed. It can be seen that our model corresponds to a Al_2O_3 substrate on which has been deposited a finite film of GaN. The right panel shows the same as the left, but as a slice through the interface region in the [0 0 0 1] direction revealing the GaN surface and network of three crossing line dislocations (cf figures 2(*a*) and 3(*b*)). Residual stresses arising in the interface region are given in figure 7. These results indicate that a honeycomb network of misfit dislocations arising from the lattice mismatch between GaN and Al_2O_3 is energetically stable.

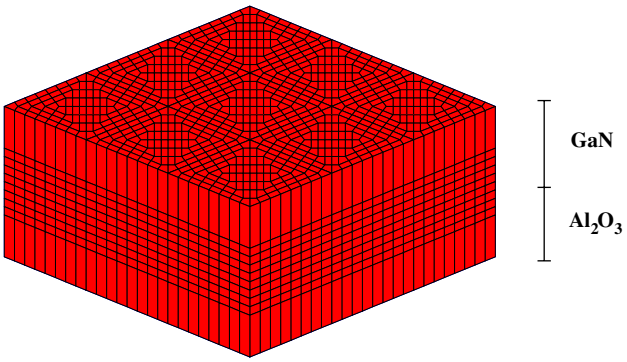

Figure 5. Graphical representation of the finite element mesh where 27-node Lagrangian elements reflect the global honeycomb structure through a coset decomposition of the primitive unit-cell described in section 4.2 (cf figure 3).

To measure the effectiveness of the methodology prescribed in this work we compare the strain values of the dislocation network relaxed by the FE method with those observed in experiment. Figure 8 illustrates strain field components obtained from the experimental image of figure 1, as well as from the FE model of the misfit dislocation system focusing on a single dislocation along the same projection direction as in the experimental image. A comparison of the two fields at a radius of 1 nm from the dislocation core yields agreement to within a typical error of 4% which is reasonably good taking into account the various cumulative experimental as well as theoretical sources of error. Closer to the core larger deviations are obtained since the FE method employed here cannot easily treat these singularities without more direct information based on interatomic interactions.

7. Discussion and conclusions

The aim of this paper was to achieve modelling of a network of misfit dislocations by a continuum approach with FE analysis and to compare the relaxed strain energy obtained from the modelling with that obtained experimentally. The continuum model used in this work has the significant advantage of treating large volumes without utilizing millions of atoms in the formalism while providing an understanding of defect interactions. The input required is an initial 3D topological bicrystal model. As a realistic example of this we have investigated the strain response affected by misfit dislocations in the (0 0 0 1) GaN/Al_2O_3 bicrystal.

In the following, possible limitations of our approach are discussed: Our method is based on topological modelling for which input data are taken from HRTEM. Thus the absence

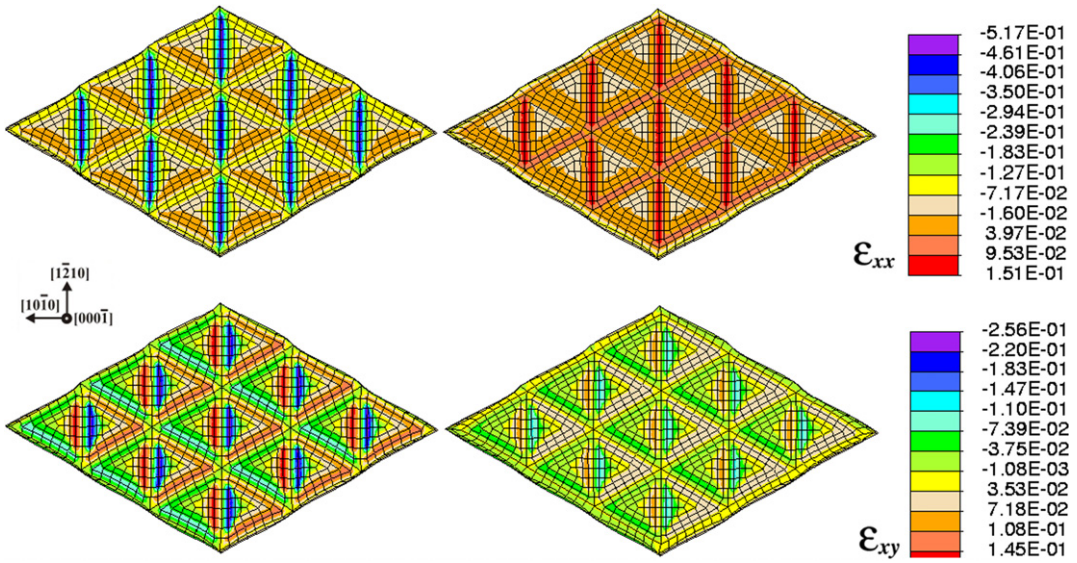

Figure 6. A cross-section through the [0 0 0 1] direction revealing relaxed honeycomb strain fields on (left) Al_2O_3 and (right) GaN surface.

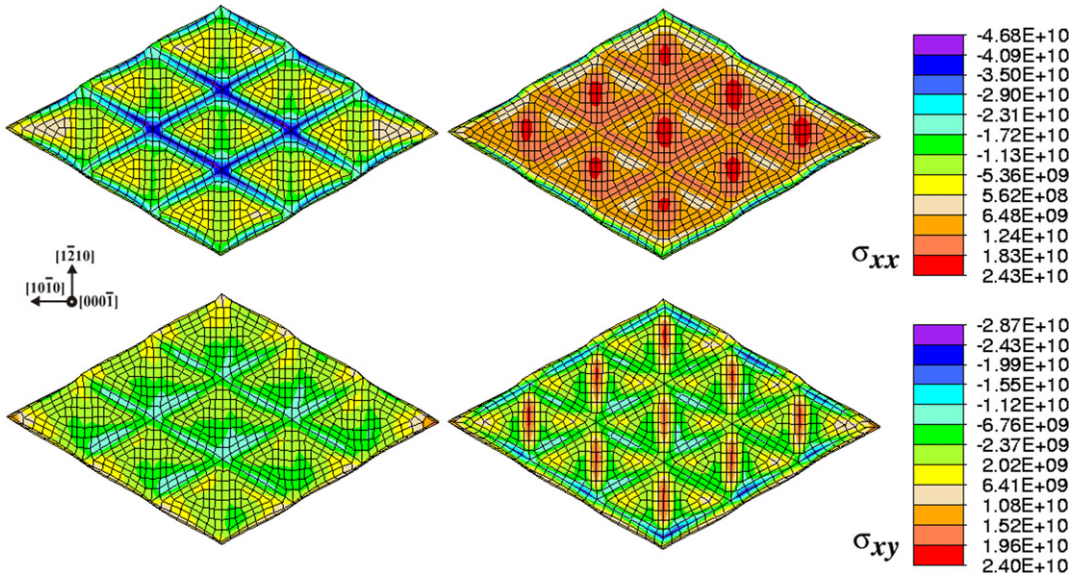

Figure 7. Same as in figure 6 but for residual stress fields. Units are in pascals.

of multiple line or planar defects at the area of interest is a necessity. Moreover, sharp and abrupt planar interfaces, lack of large concentration of impurities and well defined crystal structures are obligatory. In addition for the GPA analysis of HRTEM images the limitations discussed by Hÿtch *et al* are applicable [23].

One may also wonder on what would be the influence of inclined misfit dislocations, at 60°, on the 2D HRTEM projections and GPA maps and how such influence is taken into account in our methodology. To avoid initially this problem we chose to 'cut' the network of misfit dislocations on their nodes thus excluding the influence of the inclined line defects. However, image simulations (to be presented elsewhere) of projections with the misfit dislocations network being cut in various other positions show that the HRTEM images are little or not at all affected by the inclined dislocations because they do not yield extra half-planes in the projection direction. If any such effect exists we postulate that they are below the resolving capacity of GPA.

Another issue concerns the influence of surface relaxation effects and whether these should be taken into account. An end-on dislocation in a thin TEM foil is similar to a dislocation in a plate with parallel free surfaces. The finite thickness gives rise to elastic forces that axially twist the dislocation at the two free surfaces by equal and opposite amounts. This is the so-called Eshelby twist [24]. This relaxation effect was not taken into account in the construction of the 3D atomic configuration (figures 2 and 4). GPA, under certain conditions, is able to measure the continuous displacement fields to an accuracy of 0.03 Å, with respect to anisotropic elastic theory, without taking into account Eshelby twist. For GPA thin film relaxation is not a significant error factor, as long as no significant modification of the displacement field is observed as a function of distance from the core [12].

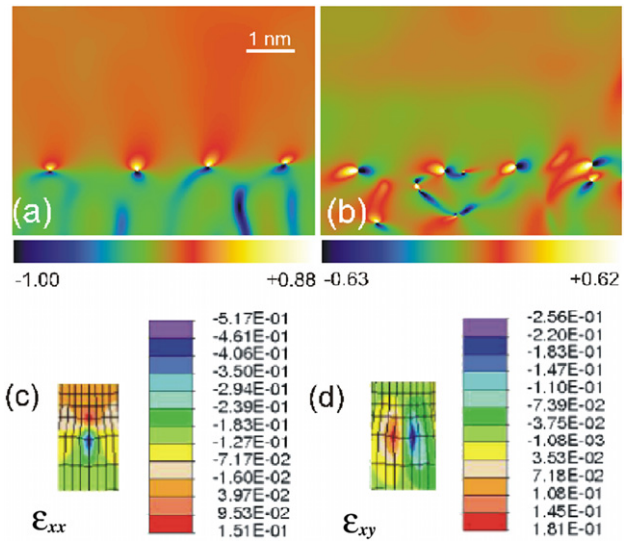

Figure 8. (*a*) and (*b*) the strain field components $\boldsymbol{e}_{xx}$ and $\boldsymbol{e}_{xy}$, respectively, calculated by GPA from the experimental HRTEM micrograph (see bounding box of figure 1). (*c*) and (*d*) the same strain field for a single misfit dislocation (area 2 nm×3 nm) centred around a misfit dislocation as calculated by FE analysis, illustrated along the same projection direction as in the experimental image.

Regarding the maximum density of misfit dislocations that can be treated by the present approach, and by setting aside the previous limitations, probably only the interaction of nonelastic core regions could not be described and consequently limit the present approach. In the present approach, we also postulate that the atomic relaxation at the core regions is not a significant error since the FEs employed here are not of atomic dimensions.

In conclusion, it has been shown that the methodology used here has the potential to simulate in 3D the strain behaviour of nanoscale materials starting only from 2D strain images and a topological model. The method we have used here is not restricted to HRTEM nor atomic imagery as a starting point, but also to any other experimental or theoretical images from which one may extract distortion maps. Nor are we strictly confined to continuous mappings since, by careful use of the MOMS interpolation scheme, we have illustrated a practicable method for dealing with singular points arising from dislocation cores.

The multi-step method we have employed here is not limited to a traditional film/substrate system and can be easily extended to include more complex structures, such as multilayers for example. Furthermore the computational process presented here can be used hand-in-hand with other techniques of HRTEM interpretation.

Acknowledgments

One of the authors (TDY) acknowledges useful technical discussion with Grzegorz Jurczak on computational details of FEA. This research was funded by the European Commission PARSEM project MRTN-CT-2004-005583 and by the Greece-Poland Joint Research and Technology programme.

References

[1] Ponce F 2000 *Introduction to Nitride Semiconductor Blue Lasers and Light Emitting Diodes* (London: Taylor and Francis)
[2] Morkoç H 2007 *Nitride Semiconductors and Devices (Springer Series in Materials Science)* 2nd edn (Berlin: Springer)
[3] Beanland R, Dunstant D J and Goodhew P J 1996 *Adv. Phys.* **45** 87
[4] Beaumont B, Bousquet V, Vennegues P, Vaille M, Bouille A, Gibart P, Dassonneville S, Amokrane A and Sieber B 1999 *Phys. Status Solidi* a **176** 567
[5] Lahreche H, Venneques P, Beaumont B and Gibart P 1999 *J. Cryst. Growth* **205** 245
[6] Jain S C, Harker A H and Cowley R A 1997 *Phil. Mag.* A **75** 1461
[7] Pond R C 1989 *Dislocations in Solids* vol 8 (Amsterdam: North-Holland)
[8] Dimitrakopulos G P, Karakostas T, Antonopoulos J G and Pond R C 1997 *Interface Sci.* **5** 35
[9] Kehagias Th, Komninou Ph, Nouet G, Ruterana P and Karakostas Th 2001 *Phys. Rev.* B **264** 195329
[10] Hÿtch M J, Snoek E and Kilaas R 1998 *Ultramicroscopy* **74** 131
[11] Stadelmann P A 1987 *Ultramicroscopy* **74** 131
[12] Hÿtch M J, Putaux J-L and Pénisson J-M 2003 *Nature* **423** 270
[13] Georgakilas A, Ng H M and Komninou Ph 2003 *Nitride Semiconductors—Handbook on Materials and Devices* (New York: Wiley-VCH)
[14] Wright A F 1997 *J. Appl. Phys.* **82** 2833
[15] Graham J 1960 *J. Phys. Chem. Solids* **17** 18
[16] Pond R C and Vlachavas D S 1983 *Prec. R. Soc. Lond.* A **386** 95
[17] Dłużewski P 2000 *J. Elasticity* **60** 119
[18] Dłużewski P, Jurczak G and Antunez H 2000 *CAMES* **10**
[19] Dłużewski P, Maciejewski G, Jurczak G, Kret S and Laval J-Y 2004 *Comput. Mater Sci.* **29** 379
[20] Dłużewski P and Traczykowski P 2003 *Arch. Mech.* **55** 501
[21] Dłużewski P and Rodzik P 1998 *Appl. Mech. Eng.* **160** 325
[22] Meijering E H W, Niessen W J and Viergever M A 2001 *Med. Image Anal.* **5** 111
[23] Hÿtch M J and Plamann T 2001 *Ultramicroscopy* **87** 199
[24] Eshelby J D and Stroh A N 1951 *Phil. Mag.* **42** 1401